

Article

Acoustic Noise Reduction in an 8/6 Switched Reluctance Machine Using Structural Design

Francisco Juarez-Leon ^{*}, Nathan Emery and Berker Bilgin 

McMaster Automotive Resource Centre (MARC), McMaster University, Hamilton, ON L8S 4L8, Canada

^{*} Correspondence: juarezlf@mcmaster.ca

Abstract: Today, switched reluctance motors (SRMs) represent a promising technology for the long-term sustainability of electrified transportation, mainly due to their simpler structure, lower production cost, and robust configuration compared to other motor technologies. Notwithstanding, high acoustic noise and torque ripple are two performance imperfections that have prevented the widespread implementation of SRMs. This paper presents different structural design techniques to reduce the acoustic noise of an 8/6 SRM, while maintaining the electromagnetic performance of the machine. For each technique, a corresponding multiphysics FEA analysis of the motor's performance is presented. The accuracy of the multiphysics model is confirmed experimentally using acoustic noise measurements obtained from a four-phase 8/6 SRM. Then, several structural techniques have been investigated on the 8/6 SRM represented in two main categories: stator-housing modifications and rotor modifications. The best design strategies are then combined to improve the acoustic noise level of the 8/6 SRM while maintaining its performance.

Keywords: acoustic noise reduction; finite element analysis; modal analysis; structural design; switched reluctance motor



Citation: Juarez-Leon, F.; Emery, N.; Bilgin, B. Acoustic Noise Reduction in an 8/6 Switched Reluctance Machine Using Structural Design. *Energies* **2023**, *16*, 3282. <https://doi.org/10.3390/en16073282>

Academic Editors: Anibal De Almeida and Lorand Szabo

Received: 14 January 2023

Revised: 31 March 2023

Accepted: 3 April 2023

Published: 6 April 2023



Copyright: © 2023 by the authors. Licensee MDPI, Basel, Switzerland. This article is an open access article distributed under the terms and conditions of the Creative Commons Attribution (CC BY) license (<https://creativecommons.org/licenses/by/4.0/>).

1. Introduction

As the impact of climate change has grown in recent years, the world has experienced a shift towards greener technologies mainly guided by the urgent need to reduce daily energy consumption levels. In the particular case of the automotive industry, several efforts have been made to move from traditional fossil-fuel-powered internal combustion engines to the electrification of vehicles, aiming to find new long-term solutions to decrease greenhouse gas emissions.

In today's market, the most popular option for traction motors in electric vehicles (EVs) are interior permanent magnet synchronous motors (IPMSMs), due to their high efficiency at low- to medium-speed range and their ability to achieve high torque density [1,2]. Although IPMSMs provide good performance and have many benefits, they suffer from major disadvantages due to the use of rare-earth permanent magnets. The performance of these magnets is strongly dependent on temperature, and they have a highly volatile and unreliable price and supply chain [1,3–6]. A second option for traction motors in EVs is the use of induction motors (IMs), also known as asynchronous machines [2]. An induction motor does not require permanent magnets, but it has conductors on the rotor. Hence, IMs can suffer from high copper losses that might require rotor cooling in propulsion applications [7].

A potential technology to sustain the demand for electrified transportation in the long-term is switched reluctance motor (SRM). SRMs do not require rare-earth magnets or conductors on the rotor. Due to their simple and robust construction, they can operate at high speeds and high temperature conditions. SRMs also have a fault tolerance capability as the phases are electrically isolated from each other [8]. The simple geometry of SRMs also reduces manufacturing complexity and allows for relatively lower production costs.

Recent research within the field of SRMs has demonstrated that this motor technology has the capability to replace current commercial motors, while achieving comparable torque/speed and efficiency features [9–12].

Historically, high torque ripple and radial forces that result in vibration and acoustic noise have been the major deterrent for SRMs [6,13,14]. Acoustic noise and vibration are present in all motor technologies, but they are more pronounced in SRMs due to their construction and excitation principles [15–17]. However, acoustic noise can be reduced significantly by applying techniques related to current control and structural design.

Most of the current control techniques applied to PMSMs and IMs for acoustic noise reduction rely on the modification of the PWM strategies that allow for selective acoustic harmonic reduction [18–20]. Control strategies for low-noise SRMs can be categorized depending on the type of the electromagnetic force to improve: radial or tangential [21]. To improve radial forces, it is possible to use independent control of pole currents, sinusoidal excitation, hybrid excitation, or a two-stage commutation [22]. On the other hand, to improve tangential forces, the control stage of an SRM drive can make use of current and angle modulation, average torque control, direct torque control, torque sharing functions (TSFs), feedback linearization control, iterative learning control, and intelligent control. Model predictive control for SRMs has also been reported in the literature [23–25].

Structural design techniques for PMSMs and IMs have also been studied for vibration and acoustic noise reduction. In [26], rotor skewing, slot bridges, and dummy slots were investigated for a PMSM, showing that adding slot bridges had the best acoustic noise performance. Slot/pole combination and winding configurations have also been analysed in [27], showing that configurations with higher vibration modes have better performance in terms of acoustic noise. In [28], mechanical modifications on the stator teeth and stator yoke thickness to improve the overall stiffness and stability of the stator core can reduce vibration and acoustic noise in an IPMSM. Rotor notching and rotor skewing techniques have also been studied for IMs in [29,30].

This paper proposes different structural design techniques to decrease the acoustic noise level generated by an 8/6 SRM, while maintaining the electromagnetic (EM) performance of the motor. Firstly, a detailed study of the active research in SRM acoustic noise reduction from the structural design aspect is presented in Section 2. Section 3 introduces a comprehensive multiphysics model developed to analyse the vibration and acoustic noise behaviour of an SRM for various structural changes under dynamic excitation. To validate the multiphysics model, numerical and experimental results for an actual four-phase 8/6 SRM are presented and compared. In Section 4, mechanical dimensions, and static and dynamic characteristics of the baseline 8/6 SRM are presented. Then, in Sections 5 and 6, different mechanical design techniques for stator and rotor, respectively, are analysed, compared, and implemented. The performance of the SRM is investigated both for acoustic noise and electromagnetic performance. Section 7 extends upon the most effective structural design methods and applies them to the baseline 8/6 SRM with further modifications to reduce the noise level. Finally, conclusions are presented in Section 8.

2. Mechanical Design Techniques for SRM Acoustic Noise Reduction

The mechanical modifications in the design of an SRM represent a multi-faceted problem, where many factors need to be considered. When targeting acoustic noise and vibration reduction with modifications in the motor's mechanical structure, the performance of the machine cannot be ignored. Mechanical design techniques can be organized into three general categories as depicted in Figure 1: stator and rotor design, machine topology, and damping techniques.

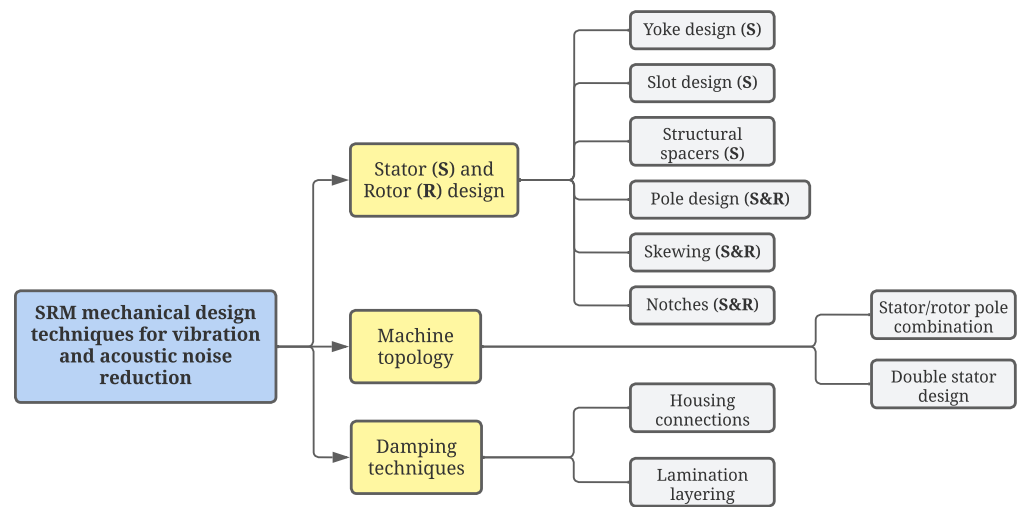


Figure 1. Overview of mechanical design techniques for vibration and acoustic noise reduction.

2.1. Stator and Rotor Design

According to Figure 1, various design changes can be applied to the stator and rotor of an SRM. Some of these modifications apply strictly to the stator (S), while most of them can be applied to both the stator and the rotor (S&R). For classification of these methods, Figure 2 outlines the typical dimensions of an SRM. The shape and size of the stator yoke can be modified to improve the structural stiffness [31–35]. Additionally, in [31,34], various shapes and designs of the stator slots were compared to investigate their impact on stator deformation. Slot wedges, which can be used in an SRM for coil retention, can be enhanced using stiff dielectric materials (structural spacers) such as alumina and polyvinyl chloride to improve the stator stiffness [35,36]. The stator and rotor poles can be designed to minimize the radial electromagnetic forces [31,32,34,37]. Notably, these structural modifications can significantly decrease the motor performance if they are applied only for acoustic noise reduction as the main objective. Stator pole modifications can be categorized as optimizing the stator taper angle and adjusting the profile of stator tooth shape.

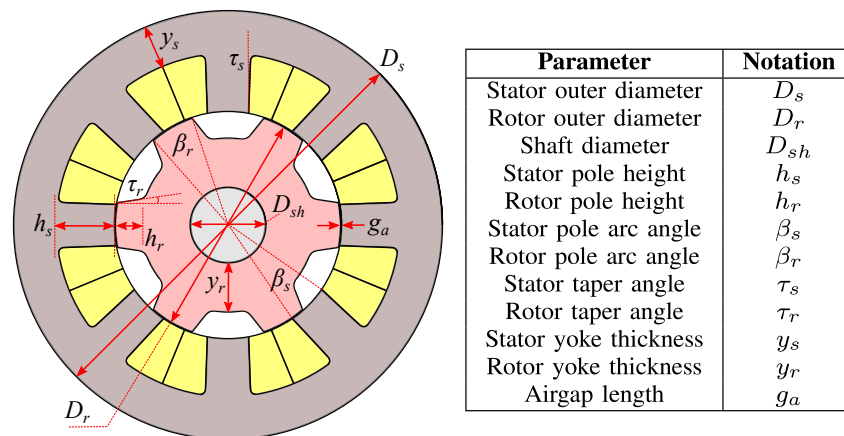


Figure 2. Terminology for typical SRM dimensions.

Rotor modifications can be categorized as introducing a curvature to the conventional extrusions of the rotor poles as outlined in Figure 3 [34,37]. These rotor modifications reduced the radial forces of the SRM and, hence, acoustic noise while preserving efficiency with less than 0.5% reduction. This type of design modification aims to change the characteristics of the radial and tangential magnetic flux density near the airgap to reduce the magnitude of the radial forces.

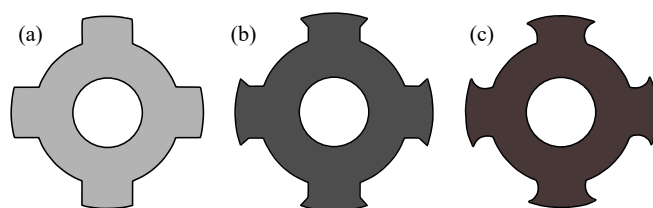


Figure 3. Comparison of rotor pole topologies: (a) conventional, (b) design from [37] to reduce radial forces, and (c) improved design from [34].

Skewing can also be applied to either the stator or rotor. Skewing techniques aim to distribute the radial force density along the stator teeth circumferentially and axially, to reduce vibration. Several studies have reported that introducing a skew angle can effectively reduce acoustic noise [38,39]. For instance, in [13], adding a higher value of rotor skewing can further minimize the acoustic noise in an SRM compared to that of a stator-skewing; however, skewing the stator and rotor together by an equal amount is the most effective design method to achieve acoustic noise reduction while maintaining the electromagnetic performance of the motor. In general, the effectiveness of skewing depends on the motor design, and operational and current control requirements. Notches can also be introduced to the rotor and/or stator to reduce acoustic noise. In [31,37,40–43], different types of notches were considered either on the rotor or stator of a corresponding SRM, taking into account various shapes and locations. When applying these techniques, the performance of the motor must be observed closely as the notches can change the flux linkage characteristics of the machine. Figure 4 shows some of the designs that were investigated for the rotor of an SRM.

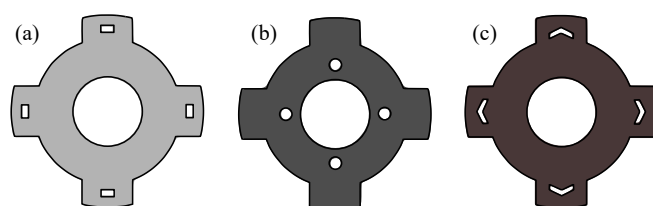


Figure 4. Rotor notch designs for acoustic noise reduction: (a) square notches [42], (b) circular notches [43], and (c) arrow notches [31].

2.2. Machine Topology

The number of poles per phase can be increased in order to reduce acoustic noise in an SRM. This might also require increasing the number of rotor poles and, hence, the number of torque pulsations and electrical frequency. A higher number of magnetic poles increases the first non-zero dominant mode shape and helps reduce mechanical resonance [40,44–48]. Furthermore, a higher number of rotor poles than stator poles can help reduce the acoustic noise [41]. It was also reported that a double stator SRM design can decrease radial forces and help obtain a higher power density compared to conventional SRMs [49–53].

2.3. Damping Techniques

Damping techniques have also been applied to SRM designs by inserting damping materials in between stator laminations [54]. In another approach presented in [55], the contact areas and housing assembly that surrounds a motor were modified to reduce the propagation of vibrations from the stator. Finally, a detailed study of different radiating rib structures in the housing of an SRM for acoustic noise reduction was presented in [56]. It was concluded that adding a large quantity of ribs with trapezoidal cross-section with a broad top and a narrow bottom is the best choice to reduce acoustic noise and help heat dissipation considering that the amount of rib material is the same for all rib structures.

3. Multiphysics Vibroacoustic Model and Experimental Validation

To accurately model the acoustic noise behaviour of an SRM, a multiphysics model was developed in Ansys Workbench as outlined in Figure 5. The multiphysics model involves electromagnetic analysis in Ansys Maxwell, structural analysis in Ansys Modal, and vibration and acoustic noise analysis in Ansys Harmonic Response and Harmonic Acoustics.

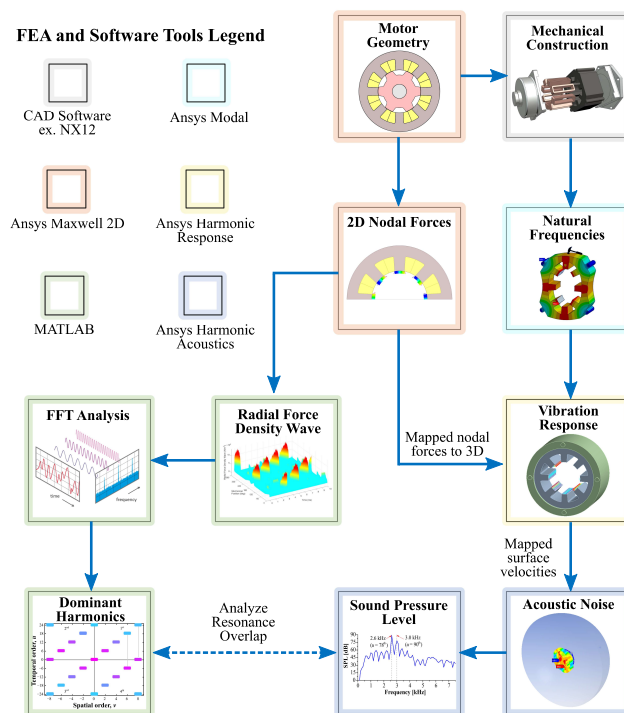


Figure 5. Block diagram of the multiphysics FEA toolchain for SRM acoustic noise analysis.

Firstly, the electromagnetic forces in the SRM are generated by applying dynamic current waveforms. Simultaneously, the structural model uses the components of the SRM assembly and material properties to calculate the dominant mode shapes and natural frequencies. Once these two analyses are completed, the electromagnetic nodal forces are mapped to the stator teeth in the structural model. A superposition of natural frequency calculations with electromagnetic nodal force harmonics in circumferential and temporal orders generates a forced vibration response of the SRM assembly. The generated velocities of the structural components serve as the input to the acoustic model. These velocities are then mapped to the components in the acoustic FEA environment, where acoustic fields and radiation boundaries are set up. Once these FEA models are coupled, the acoustic noise behaviour of the motor is calculated.

Figure 5 shows that, after completing the electromagnetic (EM) simulations, the force density waveform is exported to MATLAB for post-processing. Using the 2D FFT, the magnitudes of the circumferential and temporal radial force density harmonics are calculated. The results from the vibroacoustic FEA simulations are cross verified to see if they match with the excited natural frequencies at the dominant circumferential and temporal orders that have the same shape and forcing frequencies.

The four-phase 8/6 SRM on which the structural modifications are applied for acoustic noise reduction was modelled in the developed multiphysics vibroacoustic model and the results were validated experimentally. The 8/6 SRM is rated at 5 kW with a base speed of 6000 rpm at 300 V DC link voltage.

Figure 6a shows the experimental setup with the 8/6 SRM, an induction machine dynamometer, a four-phase asymmetric bridge converter, a microphone placed 1 m directly above the motor in the radial direction for acoustic noise measurement, and an accelerometer mounted on the outer surface of the stator for vibration measurement.

Similarly, Figure 6b shows a detailed view of the vibroacoustic measurement equipment. The sound was recorded using an audio interface, which then used a MATLAB algorithm to calculate the noise level. In order to obtain the frequency domain information, the fast Fourier transform (FFT) was applied to the measured sound pressure. The amplitude of different harmonics were then converted into decibels (dB) using:

$$\text{SPL} = 20 \log_{10} \left(\frac{\text{FFT}(P)}{P_{ref}} \right), \quad (1)$$

where P_{ref} is the reference pressure equal to $20 \mu\text{Pa}$ and P is the measured sound pressure. The stator-housing assembly was modelled to replicate the experimental setup for proper calculation of the natural frequencies. A view of the motor assembly in exploded form is shown in Figure 7.

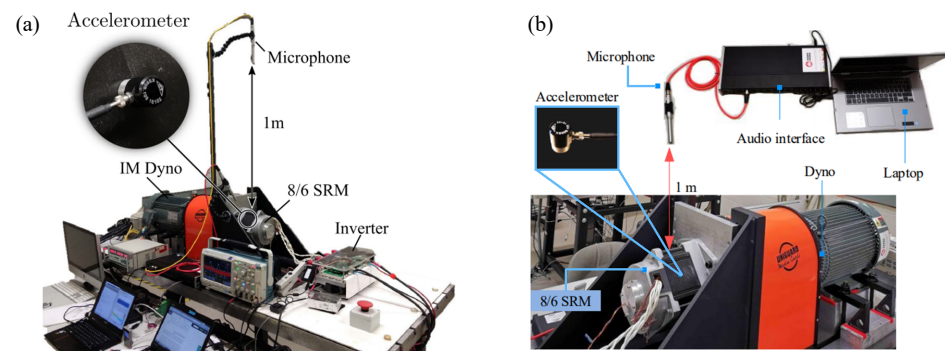


Figure 6. Experimental setup: (a) four-phase 8/6 SRM and (b) vibroacoustic measurement equipment.

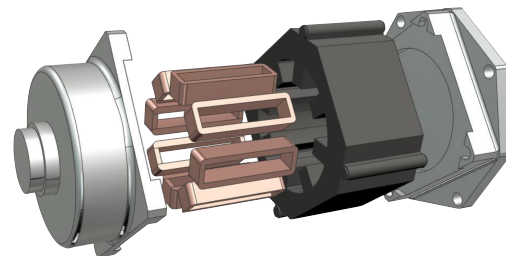


Figure 7. Stator-housing assembly CAD model for the 8/6 SRM.

The critical natural frequencies of the 8/6 SRM correspond to the shapes of the stator's vibration modes. The four-phase 8/6 SRM has two magnetic poles; hence, the natural frequency of mode shape 2 is of particular importance. Temporal orders that can excite this mode to a certain level are given by $\pm N_r + kmN_r$, with $k \in \mathbb{Z}$; where N_r is the number of rotor poles and m is the number of phases. Figure 8 shows the natural frequencies experimentally measured with an impact hammer test and the vibration modes calculated from the modal analysis in the developed multiphysics toolchain. From the finite element analysis, circumferential mode 2 and axial mode 1, e.g., (2,1) has a natural frequency of 1845.8 Hz and vibration mode (2,2) has a natural frequency of 2451 Hz. From the experimental results, the natural frequency of mode (2,1) is measured as 1884 Hz and mode (2,2) as 2435 Hz. The numerical FEA and experimental results match well.

The natural frequencies calculated using Ansys Modal are then coupled with the nodal forces simulated in Ansys Maxwell 2D. The dynamic current used for this analysis was for the operating point at 2048 rpm and 5 Nm. The multiphysics FEA simulations generate the forced vibration response and calculate the SPL produced by the motor.

The simulated SPL is then compared to the experimental SPL for a similar microphone position as in the simulation model. Table 1 shows the comparison of the simulated and experimentally measured SPL values.

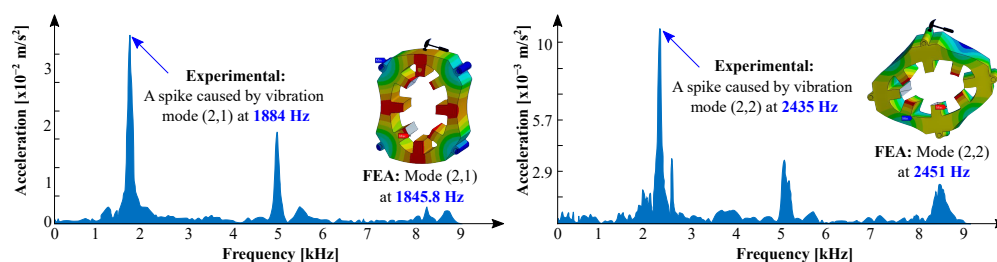


Figure 8. Impact hammer test frequency domain and FEA calculated results for vibration modes (2,1) and (2,2) [57–60].

Table 1. Comparison of SPL measured experimentally and calculated from the multiphysics toolchain.

Experimental Validation	(54th,2) 1843 Hz	(66th,2) 2253 Hz	(78th,2) 2662 Hz
Experimental results [57]	57.98 dB	46.91 dB	45.00 dB
Experimental results [59]	58.00 dB	49.00 dB	48.00 dB
FEA numerical results	63.24 dB	43.37 dB	43.42 dB

The peak SPL frequencies are due to the excitation of the dominant vibration modes (2,1) and (2,2). The forcing frequency of the radial force harmonic at 1843 Hz corresponds to the 54th temporal order and it excites the vibration mode (2,1), which has a natural frequency of 1884 Hz. Similarly, forcing frequencies 2253 Hz and 2662 Hz correspond to the 66th and 78th temporal order of the radial force harmonics and they excite the stator vibration mode (2,2).

4. Baseline Parameters of the 8/6 Switched Reluctance Motor

In this section, the baseline parameters and performance details of the experimentally characterized 8/6 SRM are presented. The static and dynamic electromagnetic characteristics, radial force, vibration, and acoustic noise performance of the baseline SRM are established. The structural modifications are applied and analysed using the developed multiphysics toolchain to improve the acoustic noise and maintain the performance with respect to the baseline parameters.

Table 2 shows the stator and rotor geometry parameters of the baseline 8/6 SRM under study, while Figure 9 shows its exploded view. In order to simplify the analysis, the motor housing is modelled as a cylindrical shell along with an endcap and a mounting plate with a similar thickness of the experimental 8/6 SRM. The fitting between the stator and the housing is modelled using interference press-fit contact, and housing and endcaps are interfaced through four bolt connections. Additionally, there are four flange mounts intended to mount the SRM on a mounting bracket or a face plate. The materials used for the motor assembly and their structural properties are listed in Table 3. Properties of the copper windings are adjusted taking into account the slot fill factor and insulation to accurately model the mass and stiffness [61].

Table 2. Baseline parameters of the four-phase 8/6 SRM.

Parameter	Symbol	Value	Unit
Number of stator poles	N_s	8	—
Number of rotor poles	N_r	6	—
Number of phases	m	4	—
Stator outer diameter	D_s	170	mm
Rotor outer diameter	D_r	89.3	mm
Shaft diameter	D_{sh}	30	mm
Stator pole height	h_s	22.3	mm
Rotor pole height	h_r	10.15	mm
Stator pole arc angle	β_s	21	deg

Table 2. Cont.

Parameter	Symbol	Value	Unit
Rotor pole arc angle	β_r	23	deg
Stator taper angle	τ_s	2	deg
Rotor taper angle	τ_r	8.5	deg
Stator yoke thickness	y_s	17	mm
Rotor yoke thickness	y_r	19.5	mm
Airgap length	g_a	0.35	mm
Fillet radius tip stator	ζ_s	0.001	mm
Fillet radius bottom stator	γ_s	2	mm
Fillet radius tip rotor	ζ_r	0.001	mm
Fillet radius bottom rotor	γ_r	4	mm
Stack length	l_{stack}	90	mm

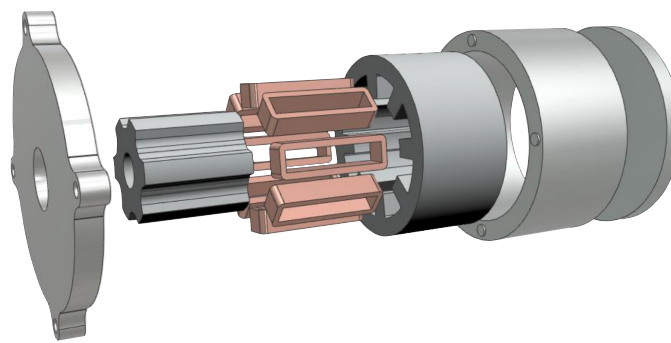


Figure 9. Exploded view of the baseline 8/6 motor assembly.

Table 3. Material properties for the baseline 8/6 SRM.

Component	Density (kg/m ³)	Young's Modulus (GPa)	Poisson's Ratio (-)
Electric steel lamination	7267.5	176	0.285
Housing and endcaps	2700	68.9	0.33
Coil windings	4908	12	0.3

Figure 10 shows the static flux linkage and torque profiles of the baseline 8/6 SRM. Figure 11 shows the dynamic phase currents and electromagnetic torque at 2000 rpm for turn-on and turn-off angles of 0 and 135 electrical degrees, respectively. The phase current reference is 21.21 A, at which the motor delivers around 7 Nm of torque with a torque ripple of 57%. The 3D assembly of the 8/6 SRM with the simplified housing (Figure 9) is modelled in the multiphysics FEA toolchain depicted in Figure 5 to calculate the natural frequency of the dominant mode shapes and vibration and acoustic noise characteristics.

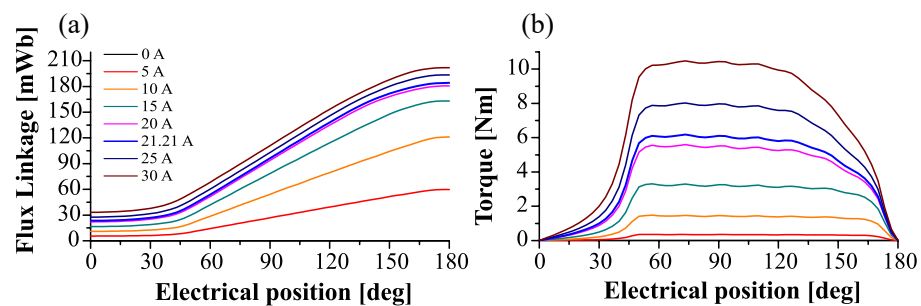


Figure 10. Static electromagnetic characteristics of the 8/6 SRM: (a) flux linkage and (b) torque.

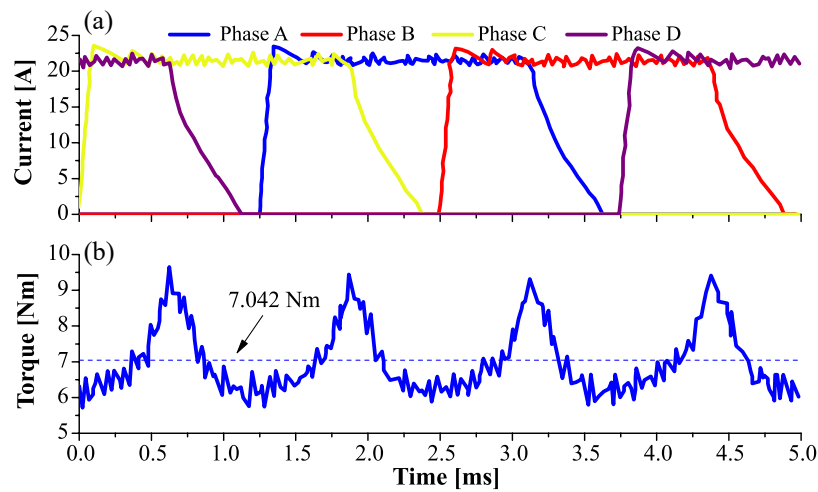


Figure 11. Dynamic results for the baseline 8/6 SRM at 2000 rpm: (a) phase currents and (b) electromagnetic torque.

As shown in Figure 12, vibration mode 2 dominates. Two frequencies were observed for mode 2 at 3030 Hz and 3551 Hz with a slight difference where the oval shape occurs. Figure 13 shows the results for harmonic response vibration analysis. The deformation pattern and stress distribution are depicted for the maximum deformation at 2600 Hz. The maximum deformation observed was 0.123 μm and the maximum stress on the stator was 0.284 MPa.

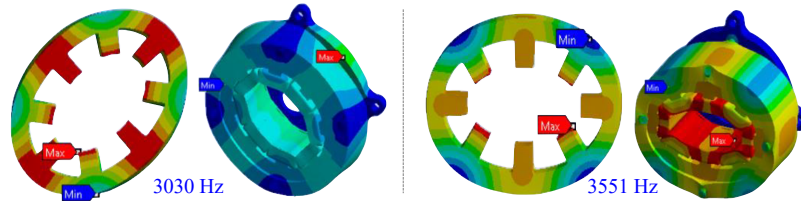


Figure 12. Mode shapes for the dominant vibration mode 2 of the baseline 8/6 SRM stator.

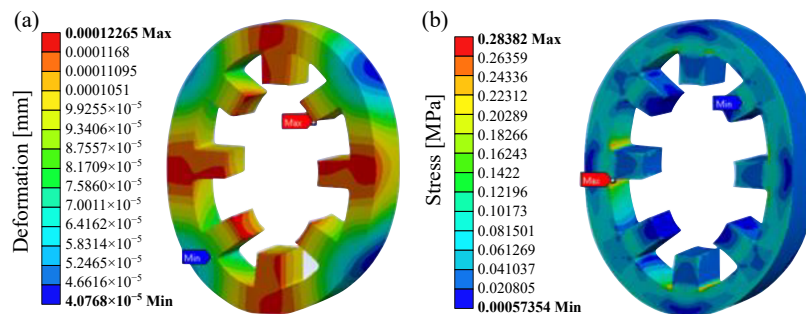


Figure 13. (a) Deformation and (b) stress contour from the forced vibration simulation at 2600 Hz.

As part of the multiphysics toolchain, the dynamic currents in Figure 11a are used in the electromagnetic FEA model to calculate the nodal forces. Nodal forces are then used to calculate the surface velocities of assembly components and acoustic noise produced by the SRM. The acoustic noise was measured from a virtual microphone positioned 1 m away from the motor assembly. Figure 14 shows the acoustic noise results for the baseline 8/6 SRM. The maximum SPL is 89.3 dB at 2600 Hz. The second SPL peak is 78.94 dB at 3000 Hz. Both of these frequencies cause acoustic noise due to excitation of vibration mode 2. The frequencies 2600 Hz and 3000 Hz correspond to the temporal orders 78th and 90th when the rotor rotates at 2000 rpm.

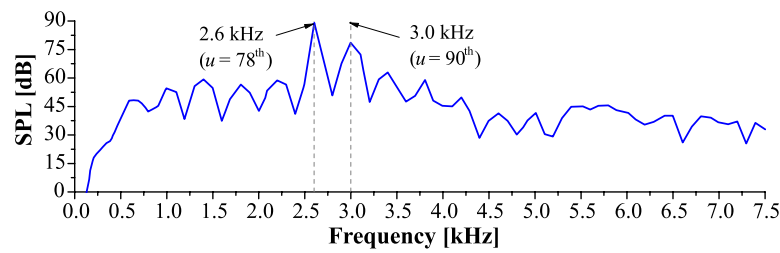


Figure 14. Sound pressure level of the baseline 8/6 SRM at 2000 rpm.

5. Stator-Housing Modifications for Acoustic Noise Reduction

The stator-housing modifications for acoustic noise reduction include variations on stator core geometry along with the housing and assembly fixtures. For the stator modifications, the main goal is to increase the stiffness of the SRM.

5.1. Stator-Housing Assembly Modifications

For the 8/6 SRM, assembly contact between the stator and the housing can be achieved using bolts or an interference fit. Table 4 shows the natural frequencies of vibration mode 2 for a press-fit assembly and a bolted assembly. The natural frequencies for the bolted assembly are 2242 Hz and 2298 Hz, while those for the press-fit assembly are 3030 Hz and 3551 Hz. Higher natural frequencies for the press-fit assembly show that it provides higher stiffness. Compared to the bolted assembly, the press-fit assembly has a larger surface area in contact between the stator and housing, which improves overall stiffness. Therefore, in the further iterations of the structural analysis of the stator, interference press-fit assembly is considered.

Table 4. Natural frequencies for the bolted and interference press-fit contacts for the 8/6 SRM.

Contact Mode	Frequencies (Hz)	Vibration Mode 2 Shapes
Bolted contact	2242	
	2298	
Interference press-fit contact	3030	
	3551	

5.2. Stator Yoke Modifications

The shape of the stator yoke influences the natural frequencies of the system along with the assembly stiffness. Various stator yoke designs are investigated as shown in Figure 15 to compare their impact, particularly to the natural frequency of the dominant vibration mode 2. The baseline stator yoke is compared with Octagon stator yokes where the vertices of the polygons are on the stator teeth as in Figure 15b and on the stator slots as in Figure 15c. Square and Hybrid Octagon structures are also investigated as shown in Figure 15d,e. A 20 mm thick housing that matches the shape of each stator yoke design is used to normalize the comparison.

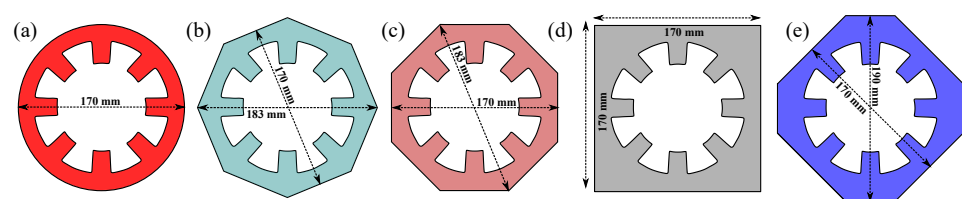
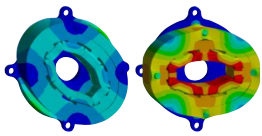
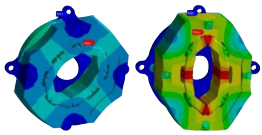
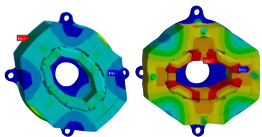
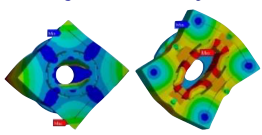
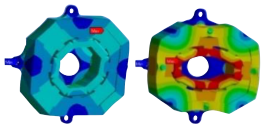


Figure 15. Stator yokes designs: (a) Baseline, (b) Octagon I, (c) Octagon II, (d) Square, and (e) Hybrid Octagon.

Table 5 shows the stator mass, natural frequencies, and vibration mode 2 shapes for the different yoke designs. Octagon II has higher natural frequencies compared to Octagon I for the same stator mass. The Hybrid Octagon structure provides higher natural frequencies as compared to Square yoke with a lower stator mass. Therefore, Octagon II and Hybrid Octagon yokes were used to compare the acoustic noise performance with the baseline design, as shown in Figure 16. Compared to the baseline design, Octagon II reduces the peak SPL from 89.30 to 76.81 dB. Both peaks occur at 2600 Hz since both designs have similar mode 2 natural frequencies. The Hybrid Octagon design reduces the maximum SPL from 89.30 to 70.28 dB. The peak SPL occurs at 3000 Hz as the mode 2 natural frequencies of Hybrid Octagon are higher than both the Octagon II and baseline designs. The two highest SPLs of all three designs correspond to 78th and 90th temporal orders of the radial force harmonic for circumferential mode 2.

Table 5. Stator yoke designs and corresponding mode 2 natural frequencies.

Design	Stator Mass (kg)	Frequencies (Hz)	Vibration Mode 2 Shapes
Baseline	7.48	3030 3551	
Octagon I	8.16	3014 3485	
Octagon II	8.16	3064 3544	
Square	11.54	3104 3450	
Hybrid Octagon	9.69	3171 3578	

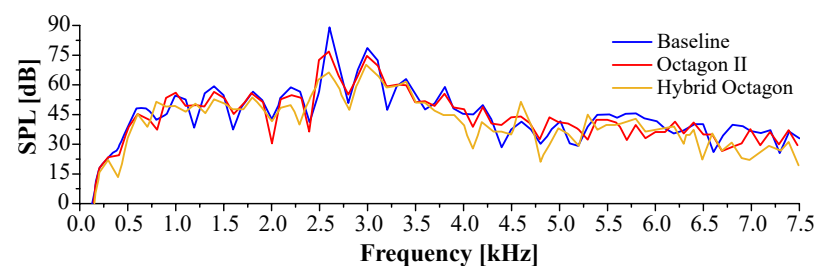


Figure 16. Total SPL comparison for Octagon II and Hybrid Octagon designs vs. Baseline.

Table 6 outlines the performance metrics for the stator yoke designs. The Hybrid Octagon design has the lowest SPL level, but it has a higher mass compared to Baseline and Octagon II designs. For each design in Table 6, the mass of the rotor and the end plates are the same. When applying the structural noise reduction methods, it is essential to improve the stiffness with the minimum increase in mass. Therefore, the torque density is considered when applying the combined structural modifications to the 8/6 SRM for acoustic noise reduction in Section 7.

Table 6. Performance comparison for the evaluated stator yoke designs.

Design	T_{ave} (Nm)	$F_{r(max)}$ (N)	Peak SPL (dB)	Total SPL (dB)
Baseline	6.998	1633.514	89.30 @ 2.6 kHz	89.89
Octagon II	7.010	1635.809	76.81 @ 2.6 kHz	80.73
Hybrid Octagon	7.011	1635.778	70.28 @ 3.0 kHz	74.40

5.3. Impact of Fasteners

To analyse the impact of housing–endplate bolted contacts on the natural frequencies of the motor assembly, the number of bolts for the baseline design was increased. Two designs used the same size of bolts but the number was increased from 4 to 8 and 16. The resultant stiffness of the system increased significantly. This can be quantified by the increase in natural frequencies with the increase in the number of bolts as shown in Table 7. The motor geometry is kept consistent to ensure that the impact on system natural frequencies are only due to the number of bolts. The increased stiffness from the higher number of bolts dramatically increases the mode 2 natural frequencies. Although the highest natural frequency would be desired, the manufacturing complexity of these designs also needs to be considered. The increase in number of bolts comes with an increase in the production and assembly cost.

Table 7. Mode 2 natural frequencies of increased bolt designs.

Design	Mode 2 Natural Frequencies
Baseline (4 bolts)	3030 and 3551 Hz
8 bolts	3486 and 3618 Hz
16 bolts	3769 and 3974 Hz

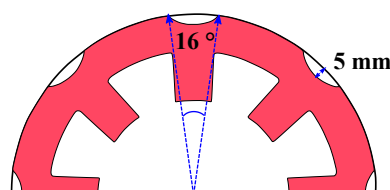
The stiffness of the system was also investigated by analysing the impact of the number of flange mount bolts on the natural frequencies. As shown in Table 8, the inclusion of four more flange mounts increases the lowest mode 2 natural frequency from 3486 to 3622 Hz, thereby reducing the excitation of vibration mode 2.

Table 8. Mode 2 natural frequencies of an additional flange mount design.

Design	Mode 2 Natural Frequencies
Baseline (4 bolts), 4 flange mounts	3030 and 3551 Hz
8 bolts, 4 flange mounts	3486 and 3618 Hz
8 bolts, 8 flange mounts	Both 3623 Hz

5.4. Stator Back Iron Notches

As shown in Figure 17, stator notches are added to the stator outer diameter facing the stator teeth. This is the shortest path for vibrations to propagate to the housing when excited by the radial forces acting on the stator teeth. The notches reduce surface area of the stator in contact with the housing at these points in attempt to reduce acoustic noise. The notches are 5 mm deep at the center of the arc with a span of 16°. The width of the notch is determined by extending the stator pole lines where they meet the stator outer diameter.

**Figure 17.** Notches added to the stator back iron of the 8/6 SRM.

As shown in Table 9, the notched design has the same average torque and slightly lower radial force, both in static and dynamic domains. Similarly, mode 2 natural frequencies for the notched design are slightly lower than those of the baseline design. Figure 18 compares the SPL for the baseline design and the design with the stator notches. The overall SPL characteristics are similar, but the maximum SPL reduced from 89.3 to 81.88 dB. This brings down the total SPL for the notched design to 84.25 dB, a 5.63 dB reduction compared to the baseline design.

Table 9. Performance comparison for the baseline and stator back iron notch designs.

Design	T_{ave} (Stat.) (Nm)	$F_{r(max)}$ (Stat.) (N)	T_{ave} (Dyn.) (Nm)	$F_{r(max)}$ (Dyn.) (N)	Mode 2 Natural Frequencies (Hz)
Baseline	4.1053	1792.01	6.9989	1633.51	3030 3551
Stator back iron notch	4.1043	1788.73	6.9955	1630.36	3028 3434

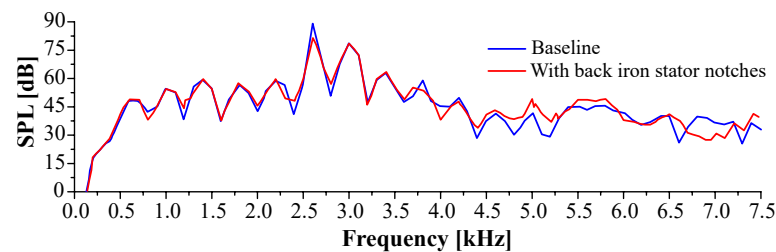


Figure 18. SPL comparison for the notched stator back iron design.

6. Rotor Modifications for Acoustic Noise Reduction

Rotor modifications include design changes that modify the electromagnetic characteristics of the motor. Therefore, they are much more sensitive to the operational characteristics of the SRM and require solutions to obtain a trade-off between acoustic noise and EM performance. These modifications include windows and notches on the rotor laminations to reduce radial forces.

6.1. Rotor Window

A rotor window is basically a flux barrier of a certain shape located on the rotor pole. The rotor window impacts the flux path and, hence, the static torque and radial force characteristics of the motor. As shown in Figure 19, five different rotor window geometries were investigated. The distance between each window and the airgap was kept constant. The dimensions of the window shapes were determined to maintain a surface area of approximately 4 mm². Static torque and radial forces for each design are depicted in Figure 20. The dip in torque profile is a result of the change in the flux distribution due to the rotor windows. To quantify the impact of a rotor window on the electromagnetic performance of the motor a performance ratio (PR) metric was used:

$$PR = \frac{\% \text{ Max. Radial Force Reduction}}{\% \text{ Avg. Torque Reduction}}. \quad (2)$$

PR allows for a comparative metric to analyse the trade-off between radial force reduction and torque loss as compared to the baseline model. A high PR ratio provides a relatively higher reduction in radial force for a lower reduction in torque. Table 10 shows the PR for the rotor window designs in Figure 19. For the same surface area and distance from the airgap, the circular window has the highest PR as it creates a smoother flux distribution around the window. The wider windows result in lower PR due to larger obstruction of the flux path.

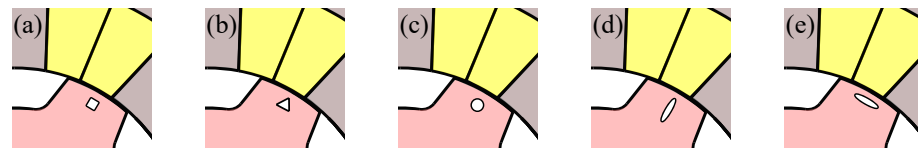


Figure 19. Various rotor window geometries: (a) Square, (b) Triangle, (c) Circle, (d) Oval I, and (e) Oval II.

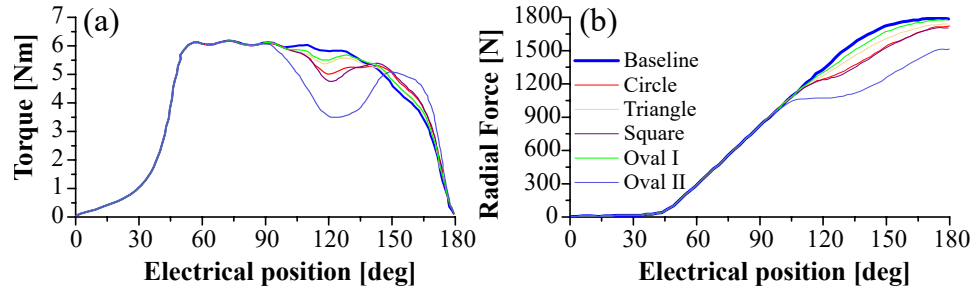


Figure 20. Rotor window performance comparisons: (a) torque and (b) radial force.

Table 10. Performance ratio comparison for various rotor window shapes.

Window Shape	Performance Ratio
Triangle	4.013
Square	3.707
Circle	4.081
Oval I	3.728
Oval II	2.248

The impact of the circular windows on the stator pole is also tested. Table 11 shows the changes in the static torque and radial force when a 1 mm radius window is located 1 mm away from the airgap either on the rotor or stator. The performance ratio is worse when the same window is applied to the stator pole only.

Table 11. Comparison of static torque and radial force reduction when a circular window is located on the rotor or stator.

Design	Torque [%]	Radial Force [%]	Performance Ratio
Rotor window	1.84	8.50	4.61
Stator Window	3.54	13.95	3.94

Additionally, the impact of the proximity to the airgap was investigated by parameterizing the distance from the center of the window to the airgap. Window size is kept the same and its position was varied from 1 to 16 mm. The analysis was conducted when the window is located on the rotor, stator, and both the rotor and the stator. Figure 21 shows the change in the static torque and radial force, and the corresponding performance ratio.

The PR for the rotor window is significantly better when it is located less than 10 mm away from the airgap. Beyond that distance, the rotor windows have negligible impact on the torque and radial force. A rotor window located at 1 mm away from the airgap, can reduce radial force by 8.5% with only 1.84% reduction in static torque in the 8/6 SRM. In comparison, when the window is located on the stator at 16 mm away from the airgap, the reduction in torque is 1.98% while the reduction in radial force is 8.05%. The same applies when both windows are located 16 mm away from the airgap.

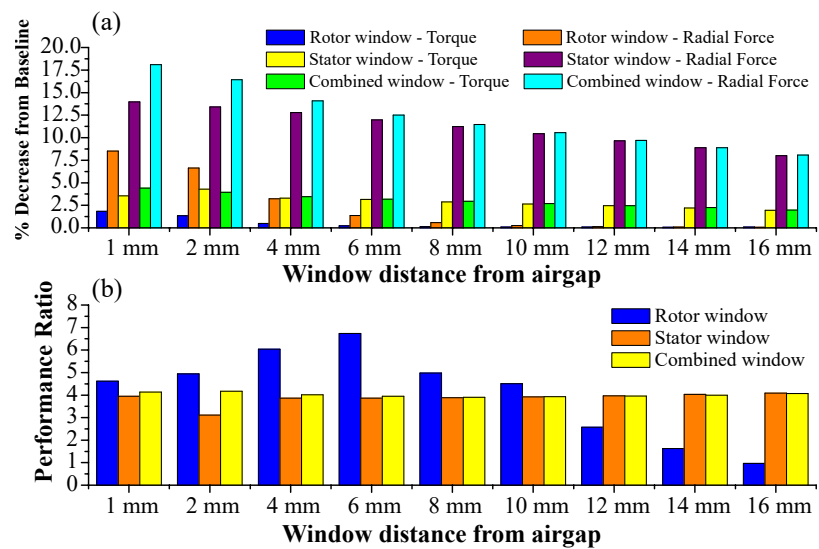


Figure 21. Rotor, stator, and combined circular window design comparisons based on the proximity to the airgap: (a) change in static torque and radial force and (b) performance ratio.

6.2. Rotor Pole Tip Modifications

Figure 22 depicts the rotor geometries investigated for rotor pole tip modifications. Notches on the rotor pole tip, rotor rib, and curved rotor pole modifications were analysed. For the surface notches, both rectangular and semi-circle shapes were used with a 2 mm wide opening and 1 mm depth into the rotor pole. Figure 23 shows the impact of rotor modifications on the static torque and radial force characteristics of the 8/6 SRM. The surface notches impact the torque significantly, as they increase the effective airgap length in the notched region. The addition of a 1 mm rotor rib, as shown in Figure 22, reduces the motor’s performance significantly. The modifications applied on the rotor pole tip are not as effective as the rotor windows. Besides, rotor rib design might require additional rotor stress analysis to ensure the structural integrity of the thin rib. The complexity involved in the shaping of the curved rotor poles would also require modification to the current control. Table 12 compares the performance ratio of these modifications.

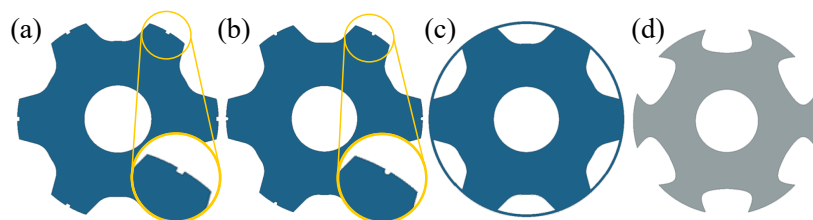


Figure 22. Rotor pole tip modifications: (a) rectangular pole surface notch, (b) semi-circular pole surface notch, (c) rotor rib, and (d) curved rotor poles.

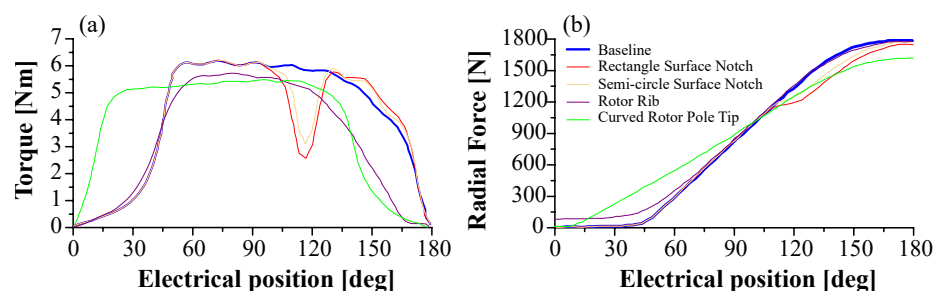


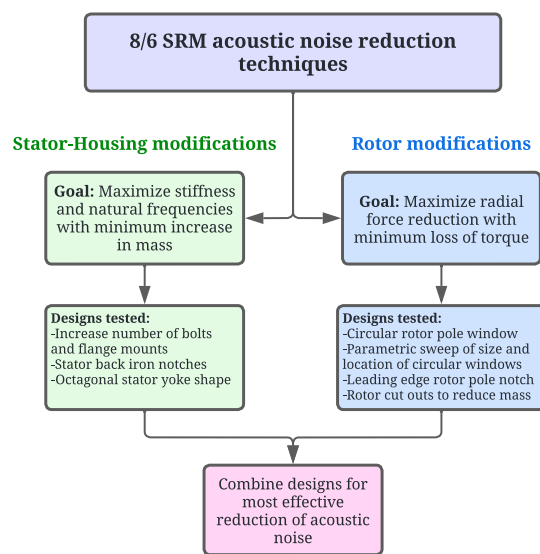
Figure 23. Comparison of motor characteristics for the rotor pole tip modifications: (a) static torque and (b) static radial force.

Table 12. Performance ratio comparison for the rotor pole tip modifications.

Rotor Pole Modification	Performance Ratio
Rectangle Surface Notch	0.563
Semi-circle Surface Notch	0.507
Rotor Rib	0.038
Curved Rotor Pole Tip	2.281

7. Acoustic Noise Reduction in the 8/6 SRM Using Structural Design Methods

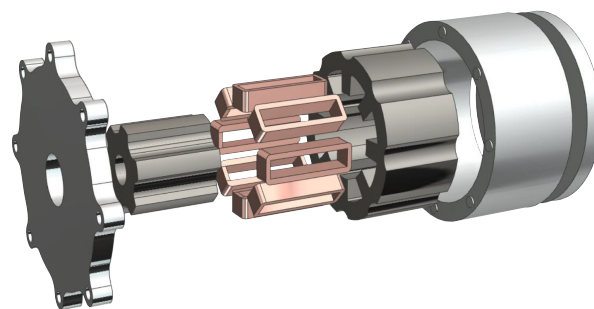
The best design techniques investigated in Sections 5 and 6 were applied to the baseline 8/6 SRM to reduce the acoustic noise production. The flowchart depicted in Figure 24 summarizes the objectives and design iterations applied to the stator and rotor of the 8/6 SRM.

**Figure 24.** Flow diagram of structural modifications applied to the 8/6 SRM for acoustic noise reduction.

7.1. Stator-Housing Modifications

7.1.1. Design I

The increase in bolts and flange mounts was combined with stator back iron notches, as shown in Figure 25. Both mode 2 natural frequencies occurred at 3492 Hz, as shown in Table 13. The natural frequency for mode 2 shapes were almost the same in Design I, because 8 bolts made the stator structure stiffer. In the baseline design with four bolts, two frequencies were observed for mode 2 at 3030 and 3551 Hz, as shown in Figure 12. This was due to the system having higher stiffness in the areas aligned with the bolts and lower stiffness in the areas that did not have the bolt support. In Design I, the support from the bolts was better aligned with the stator teeth.

**Figure 25.** Exploded view of Design I with improved bolt and flange mounts and with stator back iron notches.

7.1.2. Design II

The octagon shape was applied with the original stator outer radius of 85 mm. The back iron was increased only in the slot area as shown in Figure 15c. Similar to Design I, stator back iron notches, and 8 bolts and 8 flange mounts were included. As shown in Table 13, both natural frequencies for mode 2 shapes were increased from 3030 and 3551 Hz for the baseline design to 3588 Hz with a slight (0.39 kg) increase in stator mass.

Table 13. Design I and II mode 2 natural frequencies.

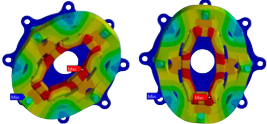
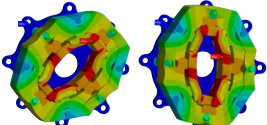
Design	Frequencies [Hz]	Vibration Mode 2 Shapes
I	3492	
II	3588	

Figure 26 shows a comparison of the acoustic noise levels for the stator-housing modifications when the dynamic operating condition of Figure 11 is used. The electromagnetic performance of the motor did not change with these modifications. The maximum SPL reduced from 89.3 dB for the baseline design to 71.24 dB for Design I and 67.78 dB for Design II. Total SPL reduced from 89.89 dB for baseline design to 76.27 dB and 73.88 dB for Designs I and II, respectively. The characteristics of the acoustic noise also changed. Due to the higher natural frequencies of Designs I and II, the maximum SPL occurs at 3400 Hz, which corresponds to 102nd temporal order of the radial force harmonic with circumferential mode 2. Table 14 provides a mass comparison for stator-housing modifications. Design II has 0.67 kg higher total mass, but it provides more significant acoustic noise reduction for the same EM performance.

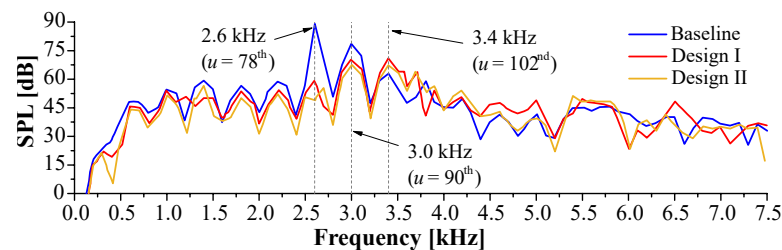


Figure 26. Acoustic noise comparison for Designs I and II.

Table 14. Designs I and II mass comparison.

Design	Rotor (kg)	Stator (kg)	Housing (kg)	Endcaps (kg)	Total (kg)
Baseline	2.84	7.48	3.36	3.79	17.47
I	2.84	7.48	3.42	3.89	17.64
II	2.84	7.87	3.53	3.89	18.14

7.2. Rotor Window Design

A parametric analysis was conducted in Ansys Maxwell 2D to determine the size and location of the rotor window. Based on the analysis presented in the previous section, a performance ratio of 4.0 or higher was targeted. Throughout the rotor window design iterations, it was observed that rotor windows might cause more significant torque reduction under dynamic operation, especially during phase commutation.

In order to minimize the average torque reduction during phase commutation, a notch on the leading edge of the 8/6 SRM was applied, as shown in Figure 27. This technique was used for torque ripple reduction in an SRM [62]. The circular window with the same dimension was offset with an angle θ towards the leading edge of the rotor in the anticlockwise direction.

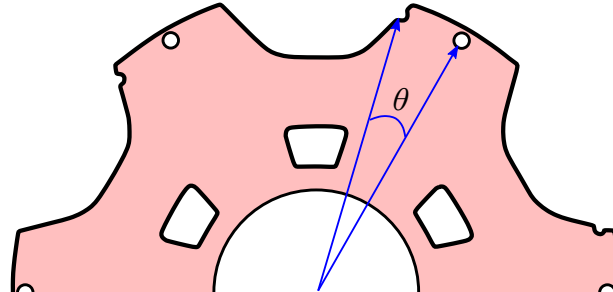


Figure 27. Rotor window and rotor notch on the leading edge of the rotor pole.

The rotor window radius was parametrically swept between 0.5 and 3 mm with an increment of 0.25 mm, and the distance from the airgap was swept between 1 and 4 mm with an increment of 0.25 mm. The offset angle, θ was parametrically swept from 11.5° from the centre of the pole to 13.5° with an increment of 0.25° . The best performance was achieved for a circular window with a radius of 1 mm at 1.75 mm away from the airgap for an offset angle of 13° . This rotor configuration results in a 16.32% reduction in radial force with a 4.07% loss in average torque, corresponding to a performance ratio of 4.01. If only the rotor circular window was used, a performance ratio of only 3.31 could be achieved.

7.3. Rotor Mass Reduction

Cut-outs are applied to the rotor to reduce the motor mass. Multiple iterations were conducted to determine the size and location of the rotor cut-outs. Figure 28 shows the cross-section view of the rotor with the cut-outs and their corresponding dimensions. The reduction in the static and dynamic torque with this modification was less than 0.1%.

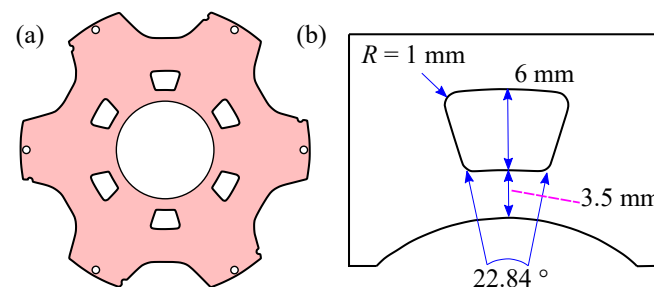
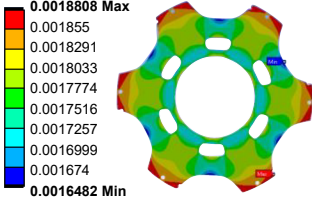
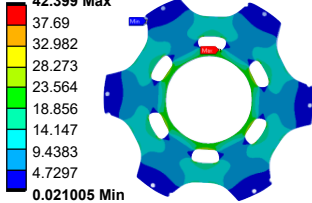
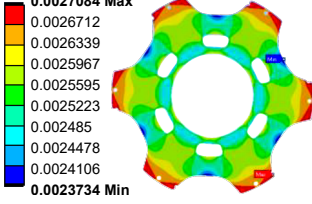
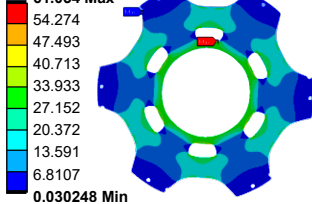


Figure 28. Rotor cut-outs for mass reduction: (a) rotor cross-section view and (b) dimensions of the cut-outs.

Rotor stress and deformation were also evaluated with the cut-outs. The baseline 8/6 SRM has a 0.35 mm airgap; therefore, the radial deformation should not exceed 0.035 mm or 10% of the airgap length. Airgap deformation can cause non-uniform radial magnetic forces, which may result in adverse motor vibrations [63]. The maximum von-Mises stress should also not exceed the yield strength of the rotor lamination material, which is 520 MPa for 35H300 electrical steel material (Nippon Steel & Sumitomo Metal Corporation) used in the baseline 8/6 SRM. Table 15 shows the results for the deformation and stress analysis with the rotor cut-outs at the maximum speed of 12,000 rpm and a burst speed of 14,400 rpm. The maximum deformation at 12,000 rpm and 14,000 rpm are 1.8 μm and 2.7 μm , and the maximum von-Mises stress are 42.39 MPa and 61.05 MPa, respectively.

Table 15. Rotor lamination deformation and stress analysis.

Speed (rpm)	Deformation (mm)	von-Mises Stress (MPa)
12,000	 <p>0.0018808 Max 0.001855 0.0018291 0.0018033 0.0017774 0.0017516 0.0017257 0.0016999 0.001674 0.0016482 Min</p>	 <p>42.399 Max 37.69 32.982 28.273 23.564 18.856 14.147 9.4383 4.7297 0.021005 Min</p>
	 <p>0.0027084 Max 0.0026712 0.0026339 0.0025967 0.0025595 0.0025223 0.002485 0.0024478 0.0024106 0.0023734 Min</p>	 <p>61.054 Max 54.274 47.493 40.713 33.933 27.152 20.372 13.591 6.8107 0.030248 Min</p>

7.4. Final Design Modifications

The stator housing assembly and rotor modifications are combined, as shown in Figure 29, and referred to as Design III. Figure 30 presents the acoustic noise, dynamic torque, and radial force characteristics of Design III. Compared to the baseline design, the maximum SPL reduced from 89.30 to 67.14 dB, which is a 24.82% reduction. The total SPL reduced from 89.89 to 72.33 dB, which is a 19.53% reduction. The total mass of the final design is 17.93 kg only 0.46 kg heavier than the baseline. The average torque at 2000 rpm reduced by 4.1% from 6.99 to 6.70 Nm. Therefore, when the stator housing assembly modifications and rotor modifications are combined, the 8/6 SRM achieves around a 20% reduction in acoustic noise with only a 4% reduction in torque.

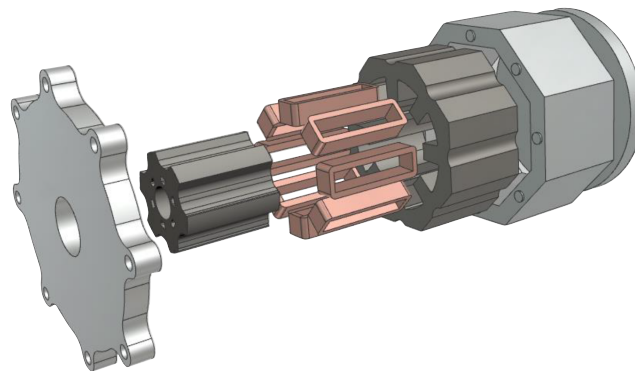


Figure 29. Exploded view of the final 8/6 SRM design with structural modifications for acoustic noise reduction (Design III).

In order to normalize the structural modifications, each design was analysed with the same current waveforms shown in Figure 11. The reduction in the average torque in Design III can be compensated by modifying the phase current waveforms. Table 16 shows the performance comparison of the structural modification evaluated for the 8/6 SRM. In Design IV, which has the same structural design as Design III, the phase current reference was increased from 21.21 A to 21.85 A for the same conduction angles to compensate the torque reduction. This results in less than a 3% increase in the RMS value of the phase current. Design IV achieves the same torque as the baseline design with a 19.48% reduction in the total SPL and with only a 2.3% reduction in torque density.

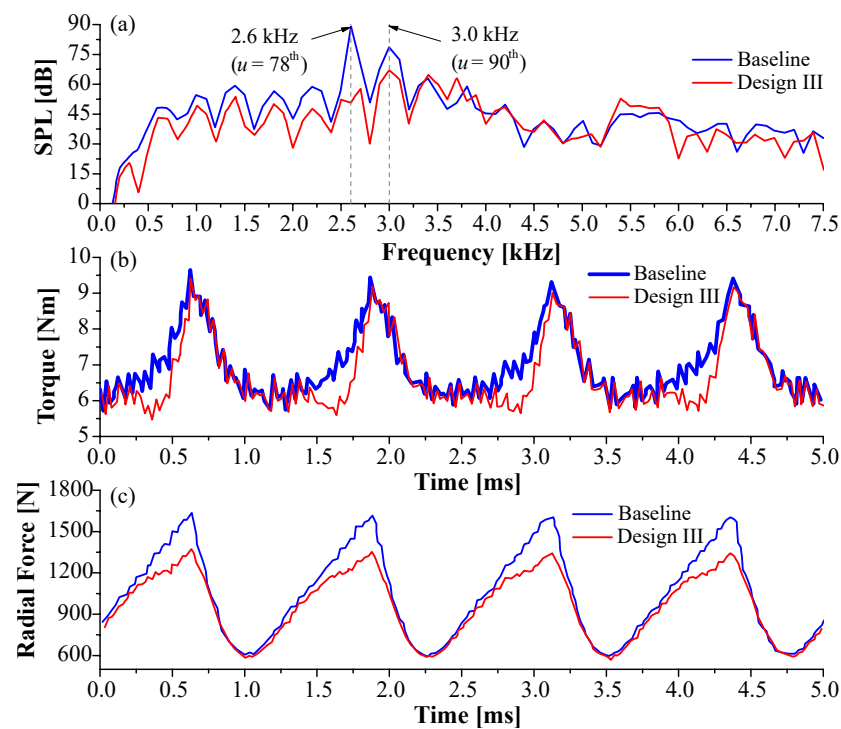


Figure 30. Comparison of performance characteristics of Design III and baseline 8/6 SRM at 2000 rpm: (a) acoustic noise level, (b) dynamic torque, and (c) radial force.

Table 16. Performance comparison of the structural modifications evaluated for the 8/6 SRM.

Design	T_{ave} (Nm)	T_{ripple} (%)	$F_r(\text{max})$ (N)	SPL (dB)	m (kg)	T_p (Nm/kg)
Baseline	6.99	57.00	1633.51	89.89	17.48	0.399
I	6.99	56.83	1632.94	76.27	17.64	0.396
II	6.99	55.99	1634.91	73.88	18.14	0.385
III	6.70	59.00	1367.24	72.32	17.94	0.373
IV	7.01	59.12	1400.93	72.38	17.94	0.390

8. Conclusions

In this paper, structural modifications were applied to a four-phase 8/6 SRM to reduce vibration and acoustic noise of the motor while maintaining the electromagnetic performance. A multiphysics modelling tool was developed to calculate the electromagnetic, modal, and acoustic noise characteristics of the motor. The tool was validated experimentally for an 8/6 SRM and the difference between the simulated and experimentally measured sound pressure level was less than 9%, 13%, and 11% for the harmonic orders 54th, 66th, and 78th, respectively. The impact of stator-housing modifications, such as the type of contact between the assembly components, stator yoke shapes, number of bolts and fasteners, and notches, were investigated on the natural frequencies of the dominant vibration mode 2 of the SRM. Then the impact of rotor modifications, such as rotor windows and notches, was investigated on the radial force and electromagnetic performance of the motor. The final design with the structural modifications on the stator and rotor achieves a 19.48% reduction in total SPL with a 2.63% increase in the total mass and less than a 3% increase in the RMS value of the phase current for the same electromagnetic torque. This shows that, by increasing the overall stiffness of the machine, a significant reduction in acoustic noise can be achieved. The motor performance can be further improved by incorporating modifications in the main dimensions of the motor core and implementing current control strategies.

Author Contributions: Conceptualization, F.J.-L., N.E. and B.B.; methodology, F.J.-L., N.E. and B.B.; software, F.J.-L. and N.E.; validation, F.J.-L. and N.E.; formal analysis, F.J.-L. and N.E.; investigation, F.J.-L., N.E. and B.B.; resources, B.B.; writing—original draft preparation, F.J.-L. and N.E.; writing—review and editing, F.J.-L. and B.B.; visualization, F.J.-L.; supervision, B.B.; project administration, B.B.; funding acquisition, B.B. All authors have read and agreed to the published version of the manuscript.

Funding: This research was undertaken, in part, thanks to the funding from the Natural Sciences and Engineering Research Council of Canada (NSERC).

Data Availability Statement: Not applicable.

Acknowledgments: The authors gratefully acknowledge Ansys for their support with Ansys Workbench 2022 R2, Ansys Electronics 2022 R2, and Ansys Mechanical 2022 R2 and CMC Microsystems for their support with SolidWorks 2022 in this research.

Conflicts of Interest: The authors declare no conflict of interest.

Abbreviations

The following abbreviations are used in this manuscript:

EV	Electric vehicle
FEA	Finite element analysis
FFT	Fast Fourier transform
IM	Induction motor
IPMSM	Interior permanent magnet synchronous motor
SPL	Sound pressure level
SRM	Switched reluctance motor

References

1. Bilgin, B.; Jiang, J.; Emadi, A. *Switched Reluctance Motor Drives: Fundamentals to Applications*, 1st ed.; CRC Press: Boca Raton, FL, USA, 2019.
2. Zhang, Z.; Bazzi, A.; Monte, J.D. A Novel PWM-control-based strategy for noise reduction in switched reluctance motors. In Proceedings of the IEEE Transportation Electrification Conference and Expo, Long Beach, CA, USA, 13–15 June 2018; pp. 1017–1022.
3. Bilgin, B.; Magne, P.; Malysz, P.; Yang, Y.; Pantelic, V.; Preindl, M.; Korobkine, A.; Jiang, W.; Lawford, M.; Emadi, A. Making the case for electrified transportation. *IEEE Trans. Transp. Electrif.* **2015**, *1*, 4–17. [\[CrossRef\]](#)
4. Bilgin, B.; Emadi, A.; Krishnamurthy, M. Design considerations for switched reluctance machines with a higher number of rotor poles. *IEEE Trans. Indust. Electron.* **2012**, *59*, 3745–3756. [\[CrossRef\]](#)
5. Emadi, A. *Advanced Electric Drive Vehicles*, 1st ed.; CRC Press: Boca Raton, FL, USA, 2015.
6. Takiguchi, M.; Sugimoto, H.; Kurihara, N.; Chiba, A. Acoustic noise and vibration reduction of SRM by elimination of third harmonic component in sum of radial forces. *IEEE Trans. Energy Convers.* **2015**, *30*, 883–891. [\[CrossRef\]](#)
7. Yoon, M.K.; Jeon, C.S.; Kauh, S.K. Efficiency increase of an induction motor by improving cooling performance. *IEEE Trans. Energy Convers.* **2002**, *17*, 1–6. [\[CrossRef\]](#) [\[PubMed\]](#)
8. Bilgin, B.; Howey, B.; Callegaro, A.; Liang, J.; Kordic, M.; Taylor, J.; Emadi, A. Making the case for switched reluctance motors for propulsion applications. *IEEE Trans. Veh. Tech.* **2020**, *69*, 7172–7186. [\[CrossRef\]](#)
9. Ruba, M.; Chindris, V.; Fodorean, D. Design and experimental validation of a low voltage high current SRM for light electric vehicles. In Proceedings of the International Symposium on Power Electronics, Electrical Drives, Automation and Motion, Ischia, Italy, 18–20 June 2014; pp. 118–123.
10. Urase, K.; Kiyota, K.; Sugimoto, H.; Chiba, A. Design of a switched reluctance generator competitive with the IPM generator in hybrid electrical vehicles. In Proceedings of the International Conference on Electrical Machines and Systems, Sapporo, Japan, 21–24 October 2012; pp. 1–6.
11. Kiyota, K.; Chiba, A. Design of switched reluctance motor competitive to 60-kW IPMSM in third-generation hybrid electric vehicle. *IEEE Trans. Ind. Appl.* **2012**, *48*, 2303–2309. [\[CrossRef\]](#)
12. Forsyth, A.; Juarez-Leon, F.; Bilgin, B. Sizing of a traction switched reluctance motor for an electric refuse-collecting vehicle application. *Machines* **2023**, *11*, 274. [\[CrossRef\]](#)
13. Gundogmus, O.; Das, S.; Yasa, Y.; Elamin, M.; Sozer, Y.; Kutz, J.; Tylenda, J.; Wright, R. Acoustic noise mitigation in high pole count switched reluctance machines utilizing skewing method on stator and rotor poles. *IEEE Trans. Indust. Electron.* **2022**, *69*, 5581–5593. [\[CrossRef\]](#)

14. Bayless, J.; Kurihara, N.; Sugimoto, H.; Chiba, A. Acoustic noise reduction of switched reluctance motor with reduced RMS current and enhanced efficiency. *IEEE Trans. Energy Convers.* **2016**, *31*, 627–636. [[CrossRef](#)]
15. Kumar, A.; Narayanan, G. Variable-switching frequency PWM technique for induction motor drive to spread acoustic noise spectrum with reduced current ripple. *IEEE Trans. Indust. Appl.* **2016**, *52*, 3927–3938. [[CrossRef](#)]
16. Xu, J.; Zhang, H. Random asymmetric carrier PWM method for PMSM vibration reduction. *IEEE Access* **2020**, *8*, 109411–109420. [[CrossRef](#)]
17. Lo, W.; Chan, C.; Zhu, Z.; Xu, L.; Howe, D.; Chau, K. Acoustic noise radiated by PWM-controlled induction machine drives. *IEEE Trans. Ind. Electron.* **2000**, *47*, 880–889. [[CrossRef](#)]
18. Miyama, Y.; Ishizuka, M.; Kometani, H.; Akatsu, K. Vibration reduction by applying carrier phase-shift PWM on dual three-phase windings permanent-magnet synchronous motor. In Proceedings of the IEEE International Electric Machines and Drives Conference, Miami, FL, USA, 21–24 May 2017; pp. 1–6.
19. Ruiz-Gonzalez, A.; Vargas-Merino, F.; Heredia-Larrubia, J.; Meco-Gutierrez, M.; Perez-Hidalgo, F. Application of slope PWM strategies to reduce acoustic noise radiated by inverter-fed induction motors. *IEEE Trans. Ind. Electron.* **2013**, *60*, 2555–2563. [[CrossRef](#)]
20. Marignetti, F.; Rubino, G.; Boukadida, Y.; Conti, P.; De Gregorio, F.; Iengo, E.; Longobardi, V. Noise and vibration analysis of an inverter-fed three-phase induction motor. In Proceedings of the International Symposium on Power Electronics, Electrical Drives, Automation and Motion, Sorrento, Italy, 24–26 June 2020; pp. 157–161.
21. Gan, C.; Wu, J.; Sun, Q.; Kong, W.; Li, H.; Hu, Y. A review on machine topologies and control techniques for low-noise switched reluctance motors in electric vehicle applications. *IEEE Access* **2018**, *6*, 31430–31443. [[CrossRef](#)]
22. Shin, S.; Kawagoe, N.; Kosaka, T.; Matsui, N. Study on commutation control method for reducing noise and vibration in SRM. *IEEE Trans. Ind. Appl.* **2018**, *54*, 4415–4424. [[CrossRef](#)]
23. Valencia, D.; Tarvirdilu-Asl, R.; Garcia, C.; Rodriguez, J.; Emadi, A. A review of predictive control techniques for switched reluctance machine drives. Part I: Fundamentals and current control. *IEEE Trans. Energy Convers.* **2021**, *36*, 1313–1322. [[CrossRef](#)]
24. Valencia, D.; Tarvirdilu-Asl, R.; Garcia, C.; Rodriguez, J.; Emadi, A. A review of predictive control techniques for switched reluctance machine drives. Part II: Torque control assessment and challenges. *IEEE Trans. Energy Convers.* **2021**, *36*, 1323–1335. [[CrossRef](#)]
25. Valencia, D.; Tarvirdilu-Asl, R.; Garcia, C.; Rodriguez, J.; Emadi, A. Vision, challenges, and future trends of model predictive control in switched reluctance motor drives. *IEEE Access* **2021**, *9*, 69926–69937. [[CrossRef](#)]
26. Hasan, I.; Sozer, Y.; Ortega, A.; Paul, S.; Islam, R. Investigation of design based solutions to reduce vibration in permanent magnet synchronous machines with low order radial forces. In Proceedings of the IEEE Energy Conversion Congress and Exposition, Cincinnati, OH, USA, 1–5 October 2017; pp. 5431–5437.
27. Islam, M.; Islam, R.; Sebastian, T. Noise and vibration characteristics of permanent magnet synchronous motors using electromagnetic and structural analyses. In Proceedings of the IEEE Energy Conversion Congress and Exposition, Phoenix, AZ, USA, 17–22 September 2011; pp. 3399–3405.
28. Lee, S.; Hong, J.; Hwang, S.; Lee, T.; Lee, Y.; Kim, Y. Optimal design for noise reduction in interior permanent-magnet motor. *IEEE Trans. Ind. Appl.* **2009**, *45*, 1954–1960.
29. Zhou, G.; Shen, J. Rotor notching for electromagnetic noise reduction of induction motors. *IEEE Trans. Ind. Appl.* **2017**, *53*, 3361–3370. [[CrossRef](#)]
30. Darjazini, A.; Karimi, M.; Saeedinia, M.; Cheraghi, M. Vibration and noise analysis of squirrel cage induction motors with double non-skewed rotor structure. In Proceedings of the Power Electronics, Drive Systems, and Technologies Conference, Tehran, Iran, 1–3 February 2022; pp. 212–217.
31. Sakuma, A.; Kadowaki, M.; Ukigai, H.; Miki, I.; Okamoto, T.; Segawa, T. Stator structure for noise reduction of switched reluctance motor. In Proceedings of the International Conference on Electrical Machines and Systems, Sapporo, Japan, 21–24 October 2012; pp. 1–4.
32. Hong, J.; Ha, K.; Lee, J. Stator pole and yoke design for vibration reduction of switched reluctance motor. *IEEE Trans. Magn.* **2002**, *38*, 929–932. [[CrossRef](#)]
33. Cai, W.; Pillay, P.; Tang, Z.; Omekanda, A. Low-vibration design of switched reluctance motors for automotive applications using modal analysis. *IEEE Trans. Ind. Appl.* **2003**, *39*, 971–977. [[CrossRef](#)]
34. Takayama, K.; Miki, I. Design of switched reluctance motor to reduce acoustic noise. In Proceedings of the International Symposium on Power Electronics, Electrical Drives, Automation and Motion, Capri, Italy, 22–24 June 2016; pp. 425–429.
35. Rasmussen, P.; Andreasen, J.; Pijanowski, J. Structural stator spacers—a solution for noise reduction of switched reluctance motors. *IEEE Trans. Ind. Appl.* **2004**, *40*, 574–581. [[CrossRef](#)]
36. Naderi-Samani, O.; Ganji, B. Noise reduction of switched reluctance motors. In Proceedings of the Power Electronics, Drive Systems & Technologies Conference, Mashhad, Iran, 14–16 February 2017; pp. 300–304.
37. Edamura, K.; Miki, I. Design of stator and rotor for noise reduction of SRM. In Proceedings of the International Conference on Electrical Machines and Systems, Hangzhou, China, 22–25 October 2014; pp. 1871–1874.

38. Yang, H.; Lim, Y.; Kim, H. Acoustic noise/vibration reduction of a single-phase SRM using skewed stator and rotor. *IEEE Trans. Indust. Electron.* **2013**, *60*, 4292–4300. [[CrossRef](#)]
39. Gan, C.; Wu, J.; Shen, M.; Yang, S.; Hu, Y.; Cao, W. Investigation of skewing effects on the vibration reduction of three-phase switched reluctance motors. *IEEE Trans. Magn.* **2015**, *51*, 1–9. [[CrossRef](#)]
40. Sanada, M.; Morimoto, S.; Takeda, Y.; Matsui, N. Novel rotor pole design of switched reluctance motors to reduce the acoustic noise. In Proceedings of the Conference Record of the 2000 IEEE Industry Applications Conference, Rome, Italy, 8–12 October 2000; pp. 107–113.
41. Tekgun, D. Acoustic Noise and Vibration Reduction on Switched Reluctance Machines through Hole Placement in Stator/Rotor Laminations. Master's Thesis, The University of Akron, Akron, OH, USA, 2017.
42. Elamin, M.; Yasa, Y.; Sozer, Y.; Kutz, J.; Tylenda, J.; Wright, R. Effects of windows in stator and rotor poles of switched reluctance motors in reducing noise and vibration. In Proceedings of the IEEE International Electric Machines and Drives Conference, Miami, FL, USA, 21–24 May 2017; pp. 1–6.
43. Li, J.; Sun, H.; Liu, Y. New rotor structure mitigating vibration and noise in switched reluctance motor. In Proceedings of the International Conference on Information, Networking and Automation, Kunming, China, 18–19 October 2010; pp. V2-80–V2-84.
44. Ma, C.; Qu, L. Design considerations of switched reluctance machines for structural vibration reduction. In Proceedings of the IEEE Transportation Electrification Conference and Expo (ITEC), Chicago, IL, USA, 22–24 June 2017; pp. 598–604.
45. Desai, P.; Krishnamurthy, M.; Schofield, N.; Emadi, A. Novel switched reluctance machine configuration with higher number of rotor poles than stator poles: Concept to implementation. *IEEE Trans. Ind. Electron.* **2010**, *57*, 649–659. [[CrossRef](#)]
46. Zhu, J.; Cheng, K.; Xue, X. Torque analysis for in-wheel switched reluctance motors with varied number of rotor poles. In Proceedings of the International Symposium on Electrical Engineering, Hong Kong, China, 14 December 2016; pp. 1–5.
47. Desai, P.; Krishnamurthy, M.; Schofield, N.; Emadi, A. Switched reluctance machines with higher rotor poles than stator poles for improved output torque characteristics. In Proceedings of the Annual Conference of IEEE Industrial Electronics, Porto, Portugal, 3–5 November 2009; pp. 1338–1343.
48. Yaman, S.; Chen, C.; Zhang, Z.; Krishnamurthy, M. Acoustic noise and vibration in switched reluctance machines: A comparative study of 12/8 and 8/6 topologies. In Proceedings of the IEEE International Electric Machines & Drives Conference, San Diego, CA, USA, 12–15 May 2019; pp. 1130–1137.
49. Abbasian, M.; Moallem, M.; Fahimi, B. Double-stator switched reluctance machines (DSSRM): Fundamentals and magnetic force analysis. *IEEE Trans. Energy Convers.* **2010**, *25*, 589–597. [[CrossRef](#)]
50. Isfahani, A.; Fahimi, B. Multi-physics analysis of double stator switched reluctance machines. In Proceedings of the IEEE Energy Conversion Congress and Exposition, Denver, CO, USA, 15–19 September 2013; pp. 2827–2833.
51. Cheng, H.; Liao, S.; Yan, W. Development and performance analysis of segmented-double-stator switched reluctance machine. *IEEE Trans. Ind. Electron.* **2022**, *69*, 1298–1309. [[CrossRef](#)]
52. Asgar, M.; Afjei, E. Radial force reduction in a new flat-type double-stator switched reluctance motor. *IEEE Trans. Energy Convers.* **2016**, *31*, 141–149. [[CrossRef](#)]
53. Isfahani, A.; Fahimi, B. Comparison of mechanical vibration between a double-stator switched reluctance machine and a conventional switched reluctance machine. *IEEE Trans. Magn.* **2014**, *50*, 293–296. [[CrossRef](#)]
54. Rasmussen, P.; LaBrush, E.; Andreasen, J. Interlaminated damping—A method for reduction of vibration and acoustic noise for switched reluctance machines. In Proceedings of the IAS Annual Meeting Conference Record of the 2005 Industry Applications, Hong Kong, China, 2–6 October 2005; pp. 1531–1539.
55. Hasan, I.; Sozer, Y.; Pina, A.; Paul, S.; Islam, R.; Klass, J. Stator design techniques to reduce vibration in permanent magnet synchronous machines. In Proceedings of the International Conference on Electrical Machines and Systems, Sydney, Australia, 11–14 August 2017; pp. 1–6.
56. Sun, J.; Zhan, Q.; Wang, S.; Ma, Z. A novel radiating rib structure in switched reluctance motors for low acoustic noise. *IEEE Trans. Magn.* **2007**, *43*, 3630–3637.
57. Callegaro, A.; Bilgin, B.; Emadi, A. Radial force shaping for acoustic noise reduction in switched reluctance machines. *IEEE Trans. Power Electron.* **2019**, *34*, 9866–9878. [[CrossRef](#)]
58. Callegaro, A.; Liang, J.; Jiang, J.; Bilgin, B.; Emadi, A. Radial force density analysis of switched reluctance machines: The source of acoustic noise. *IEEE Trans. Transp. Electr.* **2019**, *5*, 93–106. [[CrossRef](#)]
59. Liang, J.; Callegaro, A.; Bilgin, B.; Emadi, A. A novel three-dimensional analytical approach for acoustic noise modeling in switched reluctance machines. *IEEE Trans. Energy Convers.* **2021**, *36*, 2099–2109. [[CrossRef](#)]
60. Liang, J.; Callegaro, A.; Howey, B.; Bilgin, B.; Dong, J.; Lin, J.; Emadi, A. Analytical calculation of temporal and circumferential orders of radial force density harmonics in external-rotor and internal-rotor switched reluctance machines. *IEEE Open J. Ind. Appl.* **2021**, *2*, 70–81. [[CrossRef](#)]
61. Pupadubsin, R.; Steven, A.; Widmer, J. D.; Mecrow, B. C. Mechanical material properties for structural simulation model of switched reluctance machines. In Proceedings of the International Conference on Electrical Machines, Lausanne, Switzerland, 4–7 September 2016; pp. 2293–2299.

62. Lee, J.; Kim, H.; Kwon, B.; Kim, B. New rotor shape design for minimum torque ripple of SRM using FEM. *IEEE Trans. Magn.* **2004**, *40*, 754–757. [[CrossRef](#)]
63. Li, Y.; Chai, F.; Song, Z.; Li, Z. Analysis of vibrations in interior permanent magnet synchronous motors considering air-gap deformation. *Energies* **2017**, *10*, 1259. [[CrossRef](#)]

Disclaimer/Publisher’s Note: The statements, opinions and data contained in all publications are solely those of the individual author(s) and contributor(s) and not of MDPI and/or the editor(s). MDPI and/or the editor(s) disclaim responsibility for any injury to people or property resulting from any ideas, methods, instructions or products referred to in the content.